

## FORMATION AND PHOTOLUMINESCENCE PROPERTIES OF POROUS SILICON/COPPER OXIDE NANOCOMPOSITES FABRICATED VIA ELECTROCHEMICAL DEPOSITION TECHNIQUE FOR PHOTODETECTOR APPLICATION

B. E. B. AL-JUMAILI<sup>a,b</sup>, Z. A. TALIB<sup>b</sup>, A. RAMIZY<sup>c,\*</sup>, A. I. ALJAMEEL<sup>d</sup>,  
H. BAQIAH<sup>b</sup>, N. M. AHMED<sup>e</sup>, S. B. PAIMAN<sup>b</sup>, J. Y. C. LIEW<sup>b</sup>, H. K. LEE<sup>b</sup>

<sup>a</sup>Department of Medical Physics, College of Applied Science, University of Fallujah, Fallujah, Iraq

<sup>b</sup>Department of Physics, Faculty of Science, Universiti Putra Malaysia, Serdang, Selangor 43400, Malaysia

<sup>c</sup>Department of Physics, Faculty of Science, University of Anbar, Anbar, Iraq.

<sup>d</sup>Department of physics, College of Science, Imam Mohammad Ibn Saud Islamic University (IMSIU), Riyadh 11623, Saudi Arabia)

<sup>e</sup>School of Physics, Universiti Sains Malaysia, Penang 11800, Malaysia

Porous silicon (PS)/Copper oxide (CuO) photodetector was fabricated by incorporation of fine CuO nanoparticles synthesized via pulse laser ablation, onto PS substrate using electrochemical deposition technique. The influence of deposition current density (DC) on the structure, microstructure morphology and optical properties were studied using X-Ray diffraction (XRD), Field emission scanning electron microscope (FESEM), and photoluminescence (PL). The microstructure morphology observed using FESEM are strongly dependant on the DC. PL peak spectra was enhanced and getting narrower at high DC 14.2 mA/cm<sup>2</sup> which is candidate to photodetector device application. The diode behavior of the CuO/PS device was prominently superior compared to the PS/Si device. Also, the higher on/off ratio was observed at low bias voltage for the CuO/PS PD. These results attributed to the improved structural quality of the CuO layer deposited on the PS. The flexible three-dimensional structure of the nano-dendrites overcomes the possible lattice mismatch between CuO and Si, leading to low defect densities at the interface. The light trapping nature of the nano-dendrites also contributed to the signal enhancement.

(Received December 30, 2020; Accepted March 13, 2021)

**Keywords:** Copper nanodendrites, Porous silicon, Electrochemical deposition, Photoluminescence

### 1. Introduction

Porous silicon (PS) has attracted great attention because it has efficient photoluminescence (PL) at room temperature [1]. This behavior is ranged from red to blue spectrum according to its morphology and crystal size [2]–[5]. This property makes from it a good candidate for several applications including light emitting diode (LED), photovoltaic conversion[6], [7], photodetector [8], [9], sensors and silicon-insulator (SOL) applications [10]. Besides, PS can be used as host for metal or metal oxide ions because it has high surface area and open structure while its composite with other material display novel optical property [11], [12]. For example, PS/ZnO nanocomposite film had showed broad PL emission ( 350 – 800 nm) which accompanied by the combination between the red–orange emission from porous silicon and the blue–green emission of ZnO [5]. PS/Au nanocomposites exhibited an intense PL peak with blue shifted as the size of Au nanoparticles reduce [13]. While the blue emission of PS was enhanced with incorporation of Hf<sub>2</sub>O<sub>3</sub> in PS microcavity[14].

Several approaches have been used to incorporate metal/metal oxide onto PS substrate, which are routinely involved physical or chemical process. Electrodeposition [15], chemical vapor

---

\* Corresponding author: asmat\_hadithi@uoanbar.edu.iq

deposition (CVD) and sol-gel spin coating [16] are examples of a chemical method, while sputter deposition[12], and thermal evaporation [17] are examples of a physical method. Relatively, electrochemical deposition is an inexpensive and fast synthesis method [18]. However, the physical properties of PS composites synthesized via electrodeposition process are dependent on many parameters such as the chemical property of the semiconductor, electrolyte concentration, pH value, applied voltage or current and crystal orientation[19]–[22]. Therefore, optimization of these parameters is necessary to obtain PS composites with better physical properties.

PS/metals/metals oxide nanocomposites have been fabricated and investigated where special attention was given to PS/ZnO nanocomposites with the aim of obtaining white light emission[23]. PS/Cu nanocomposite is another important nanocomposite system with good optical and chemical characteristics [24]. The PL emission of PS coated with copper is stable even after three month of air treatment [25], while Cu/PS powder shows good electrochemical stability and has been used as glucose sensor[26].

Generally, the electrodeposition of metals includes two processes; charge transfer on the electrode at angstrom scale and mass transfer of reactants that occur and control the electrodeposits at microscale[27]. In this process the current density of electrodeposition is an important factor affecting the microstructure morphology of metal on PS [18]. The focus of this study is on the effect of deposition current density (DC) value during the electrochemical deposition of CuO on morphological and optical properties of the PS/CuO nanocomposites. In this paper, we report on the synthesis and characterization of Pt/CuO/PS/Pt Metal/ Semiconductor/ Metal photodetector (MSM-PD). The copper oxide NPs synthesized by pulsed laser ablation (PLA) in aqueous solution was deposited onto PS prepared via electrochemical deposition technique.

## 2. Experimental Method

The fabrication of PS/CuO photodetector was performed after the preparation of CuO nanoparticles by laser ablation on Cu target; and preparation of PS through electrochemical etching of Si as detailed below.

### 2.1. Preparation of Copper Oxide Nanoparticles (CuO NP)

The CuO nanoparticles were prepared by pulsed laser ablation method as detailed in our recent work as follows [28]. An intense pulsed laser beam of Nd-YAG ( $\lambda = 532$  nm) was used as an energy source. The laser was maintained at a pulse energy of 30 mJ/ pulse, with a pulse duration of 10 ns and repetition rate of 6 Hz. A high purity circular disk copper with 1 mm thickness was used as target and fixed on a vertical flat bracket in front of a laser beam in a cubic glass cell filled with a 20 mL distilled water. The laser beam was focused at the copper target for a duration of 60 min at room temperature for the ablation process, which produced a dark green colored colloidal solution with average particle size of 24.2 nm were used as intercalated particulates onto PS skeleton. Detailed of structure and phase formation of CuO nanoparticles can be found in our recent report [28].

### 2.2. Preparation of Porous Silicon

The PS substrate was synthesized via an electrochemical etching method by same procedure as detailed in our previous report [9]. The n-type Si substrates were first cleaned via sonication for 5 min in ethanol, acetone, and in a 10 wt. % hydrofluoric acid (HF). The substrates were rinsed after each sonication step with distilled water. The silicon substrate supported by aluminum plate was placed at the bottom of a cylindrical Teflon cell. The two-electrode setup include Si as anode and platinum (Pt) rod as a the cathode. A mixture of hydrofluoric acid and ethanol in a ratio of 1:4 (v/v) was used as an electrolyte. The PS was formed by applying 35 mA  $\text{cm}^{-2}$  current density for 15 min at RT. The electrolyte cell was emptied from HF solution and cleaned with distilled water to remove the reaction's by-product.

### 2.3. Fabrication of PS/Cu Nanocomposite and PS/CuO MSM PD

The fabrication of PS/Cu composite was done using electrochemical deposition. A mixture of diluted HF acid and colloid CuO-NPs were used as electrolyte solution. The PS substrate and Pt rod was immersed in the solution and acting as cathode and anode, respectively. About 15 ml of the electrolyte solution was poured into the cell for the Electrochemical Deposition (ECD) treatment. Electrochemical deposition was used to prepare the five samples. Samples (a, b, c, d and e) were prepared using deposition current density (DC) of 1.4, 2.8, 5.6, 11.4 and 14.2 mA/cm<sup>2</sup>, respectively for 10 min at RT. After deposition, the samples were washed several times by distilled water and dried in ambient air. Then, the sample that prepare at high DC 14.2 mA/cm<sup>2</sup> which is promised property for photodetector devices application was annealed in air at 350 °C for 1 hour to improve crystallinity and to form a single CuO phase as shown in Fig. 2 (b). The fabrication of the devices was finalized by metallization, where finger-shaped Pt electrodes are deposited on the top of CuO/PS sample using A500 Edward radio frequency magnetron sputtering system.

### 2.4. Characterizations

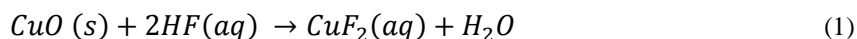
The surface morphology of the fabricated pure PS and Cu/PS composites was investigated using field emission scanning electron microscope (FESEM, JSM-7600F) attached with electron dispersive X-ray spectrometer (EDX) for elemental chemical analysis. The surface roughness was evaluated using atomic force microscopy (AFM, Bruker Dimension edge) operating in a peak force tapping mode using SCANASYST-AIR technique. The structure of samples were studied by X-ray diffraction (XRD) using PANalytical X'Pert PRO diffractometer equipped with Cu-K $\alpha$  radiation ( $\lambda=1.5418 \text{ \AA}$ ). Photoluminescence (PL) measurements were carried out on a Perkin-Elmer LS-55 spectrophotometer. The current-voltage (I-V) measurement of the fabricated devices were examined using Keithley Model 4200- Source Meter instrument. Under illumination and dark the current-voltage (I-V) and ON/OFF time characteristics were examined with 10 mW/cm<sup>2</sup> incident irradiation by the use tungsten light and the blue light ( $\lambda=460$ , intensity I=70 mW/cm<sup>2</sup>), respectively.

## 3. Results and Discussion

### 3.1. Mechanism of the Electrochemical Deposition

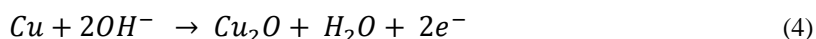
3D island growth mechanism via metals deposition onto semiconductors is affected by weak energy interaction between the metal atom adsorbed and the semiconductor[29]. In this process the electrochemical reaction caused an elevation of pH on cathode surface which is mainly attributed to water reduction [30]. This resulted in super-saturation of copper ions at the cathode neighborhood, where distinct copper phases such as Cu, CuO and Cu<sub>2</sub>O may be made onto the cathode. The value of pH in the cathode vicinity will be increased by the passage of the current from the external source to the cell, which causes the PS surface to be charged negatively. Meanwhile, the electrolyte ions of copper will relocate to cathode vicinity, and then the anions around the cathode such as OH<sup>-</sup> combined with Cu<sup>2+</sup> to form different copper phases deposit onto the surface of PS depending on their stability thermodynamically in solution [31]. The deposition is accomplished through two steps; 1) nucleation process and transformation from island deposit to continuous layer[32]. After this treatment, the color of the porous layer changed to dark red; this indicates the presence of Cu and copper oxide in the layer. Deposition of copper onto porous silicon substrate via the electro-deposition reaction can be described by the following reactions:

Step (1):



Step (2):





### 3.2. Structural analysis of PS

Fig. 1 a displays the FESEM image of PS sample prepared by electrochemical etching using current density of  $35 \text{ mA cm}^{-2}$  for 15 min. The sample exhibited uniform and large pores that has well distribution on the sample's surface. Porous layers with 85.9 % of porosity look like the ordered alternation of Si nano-branched crystals and channel voids. This property made from it perfect for deposition of Cu. Fig. 1 b illustrates the recorded EDX spectrum confirming the chemical composition of PS substrate.

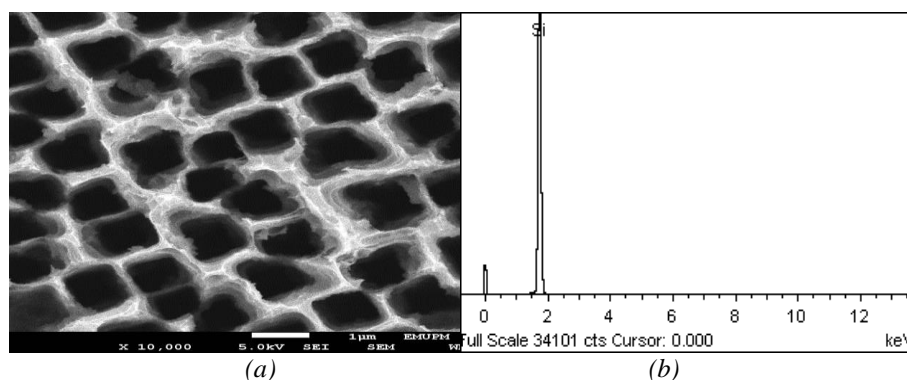


Fig. 1. (a) FESEM image and (b) EDX spectrum of PS sample prepared by electrochemical etching at current density of  $35 \text{ mA cm}^{-2}$  for 15 min.

### 3.3. Structural analysis Copper/PS Composite

#### 3.3.1. X-Ray Diffraction Patterns

Fig. 2 presents the XRD patterns of the Cu deposited into the porous Si matrix at DC = 1.4, 2.8, 5.6, 11.4 and  $14.2 \text{ mA/cm}^2$ . All the samples present sharp, narrow and well distinct peaks, which is an indication of their crystalline nature. The diffraction peaks of PS substrate dominate the overall patterns along (311) plane direction. Other XRD patterns are belong to  $\text{Cu}_2\text{O}$  and Cu matched with (ICSD, no. 98-009-5460) and (ICSD, no. 98-006-2689), respectively. The XRD peaks at  $2\theta = 43.33^\circ$ ,  $50.25^\circ$  and  $74.18^\circ$  are related to the (111), (002) and (022) planes of the pure Cu cubic structure, respectively. The weak XRD peak at  $2\theta = 36.39^\circ$  corresponding to the reflection from (111) plane of  $\text{Cu}_2\text{O}$  cubic structure. Table 1 summarizes the phase percentage of PS, Cu and  $\text{Cu}_2\text{O}$  phases calculated using Rietveld analysis. Apparently, the XRD pattern of PS was modified by varying DC during Cu deposition. In addition, the crystallite size of PS calculated using Scherrer equation decreased with increasing DC. While the phase percentage of PS decrease from 71 % for DC =  $1.4 \text{ mA/cm}^2$  to 30 % at DC =  $5.6 \text{ mA/cm}^2$  then increased to 50 and 81 % for DC = 11.4 and  $14.2 \text{ mA/cm}^2$ , respectively. On the other hand, the phase percentage and crystallites size of Cu increased with DC and then decreased at DC >  $5.6 \text{ mA/cm}^2$  (see Table 1). This indicated that at low DC =  $1.4 - 5.6 \text{ mA/cm}^2$ , thick layer was formed and cover PS crystals, while at high DC = 11.4 and  $14.2 \text{ mA/cm}^2$ , the crystallite size of Cu were decreases and their phase percentage decreased. The reduction of copper crystallite size may associate with increment of nucleation rate as well as hydrogen evolution increase. Our results agree with a previous study, which suggests that the increasing deposition current density will result in the reduction in the

particles size [13]. The presence of copper oxide in the all samples in acidic solution can be explained by Pourbaix diagram. According to a Pourbaix diagram[33], copper oxide is thermodynamically favoured in alkaline solutions (Equation 4). While Cu is favored in acidic electrolyte [34], [35] (Equation 3). In principle, the formation of copper oxide would not take place at low pH (acidic electrolyte)[31]; thus, an increase of local pH at the electrode surface (PS surface) is required to form copper oxide in acidic solution. There would be a depletion of  $H^+$  in the evolution of hydrogen, while  $OH^-$  concentration increase results from decomposition of water which consequently can result in pH increase and obtained copper oxide. Shin and co-worker obtained copper and copper oxide within anodic aluminum oxide (AAO) substrate in the electrochemical cell that is aqueous acidic, which explained by the local increase in pH at the AAO layer[36].

Fig. 2(b) shows the typical XRD pattern of a sample (sample e) annealing under 350 C for 1 h to improve crystallinity and to form a single CuO phase. The peaks observed at  $2\theta = 35.5^\circ$ ,  $38.7^\circ$ ,  $48.8^\circ$ ,  $53.4^\circ$ ,  $61.5^\circ$ ,  $66.3^\circ$ ,  $68.2^\circ$ ,  $72.4^\circ$  and  $75.2^\circ$ , are assigned to monoclinic CuO (ICSD no. 98-005-0317) along (-111), (111), (-202), (020),(202), (220), (311) and (-222) lattice planes.

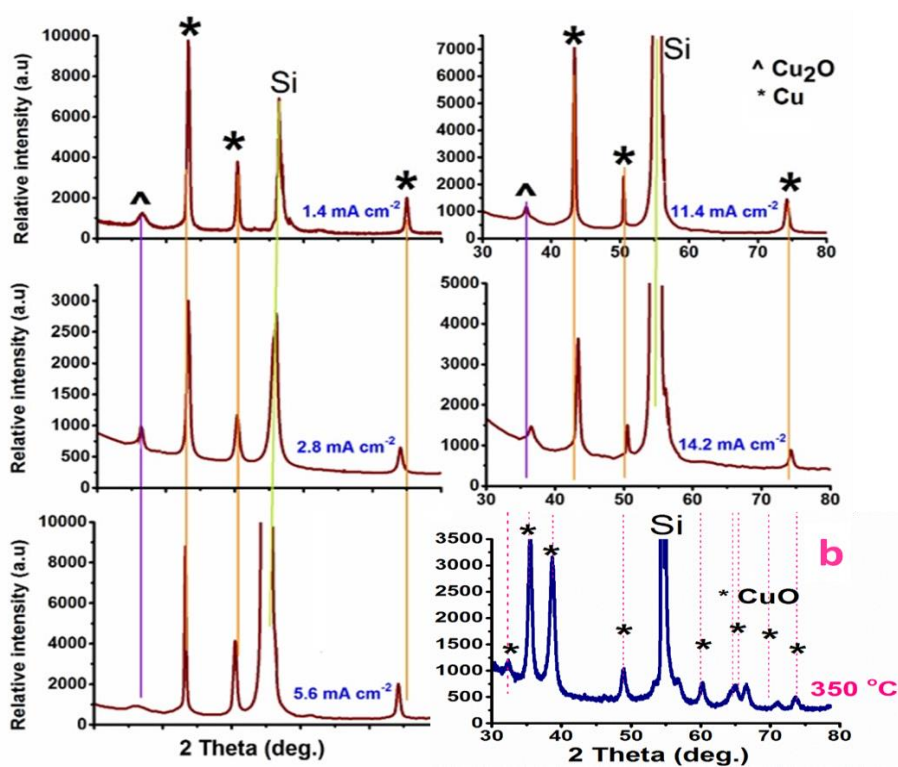


Fig. 2. XRD diffraction patterns for PS/Cu composites deposited under different current densities.

Table 1. Crystallites sizes and phase percentages of  $Cu_2O$ , Cu and PS measured from XRD and particles size and roughness of samples from AFM.

Current density (mA cm <sup>-2</sup> )	$Cu_2O$		Cu		PS	
	Crystallite size (nm)	Phases Percentage (%)	Crystallite size (nm)	Phases Percentage (%)	Crystallite size (nm)	Phases Percentage (%)
1.4	12.4	3	25.5	26	62.6	71
2.8	10	7	46.9	32	60.8	61
5.6	14.4	5	75.5	65	44.3	30
11.4	24.2	13	32.8	36	43.1	50
14.2	95	4	21.4	15	15.6	81

### 3.3.2. Field Emission Scanning Electron Microscopy

Fig. 3 displays FESEM images of the PS/Cu composites fabricated at DC = 1.4, 2.8, 5.6, 11.4 and 14.2 mA/cm<sup>2</sup>. It is noticed that the DC clearly affects the deposited layer morphology. At low DC 1.42 mA cm<sup>-2</sup>, a compact globule-like particle was formed on the top of the PS pores (Fig. 3a). When the DC was increased to 2.8 mA cm<sup>-2</sup>, a dendrites-like crystals with rod-like structures was developed as shown in Fig. 3b. By increasing DC to 5.6 mA cm<sup>-2</sup> a uniform and dendrites-like deposition was observed (Fig. 3c). Higher DC of 11.4 and 14.2 mA cm<sup>-2</sup> resulted in the formation of a well-defined branchy dendrites-like structure as illustrated in Fig. 3d and e. The formation of dendrites-like structure could be explained by the increase in hydrogen evolution at high current densities. According to Equation 5 hydrogen gas is rigorously evolved and affect the growth of copper tips. On other word, an electrolyte turbulence might be locally formed around the tips of the copper and affecting its continuous growth and promoting new nuclei formation with orientation on the tips that is random [37], [38]. Fig. 4 illustrates EDX analysis of PS/Cu composite fabricated at DC =1.4 mA/cm<sup>2</sup>. The EDX scan was taken on 5 areas including the pore and top of PS/Cu particles. The lowest weight percentage of Cu ions was in spectrum 2 and 5 that represent the interior of pore while maximum amount of Cu was on top of the PS/Cu grains. The result indicates that most of Cu ions accumulate on top of the Si silkstone and decrease inside the pore.

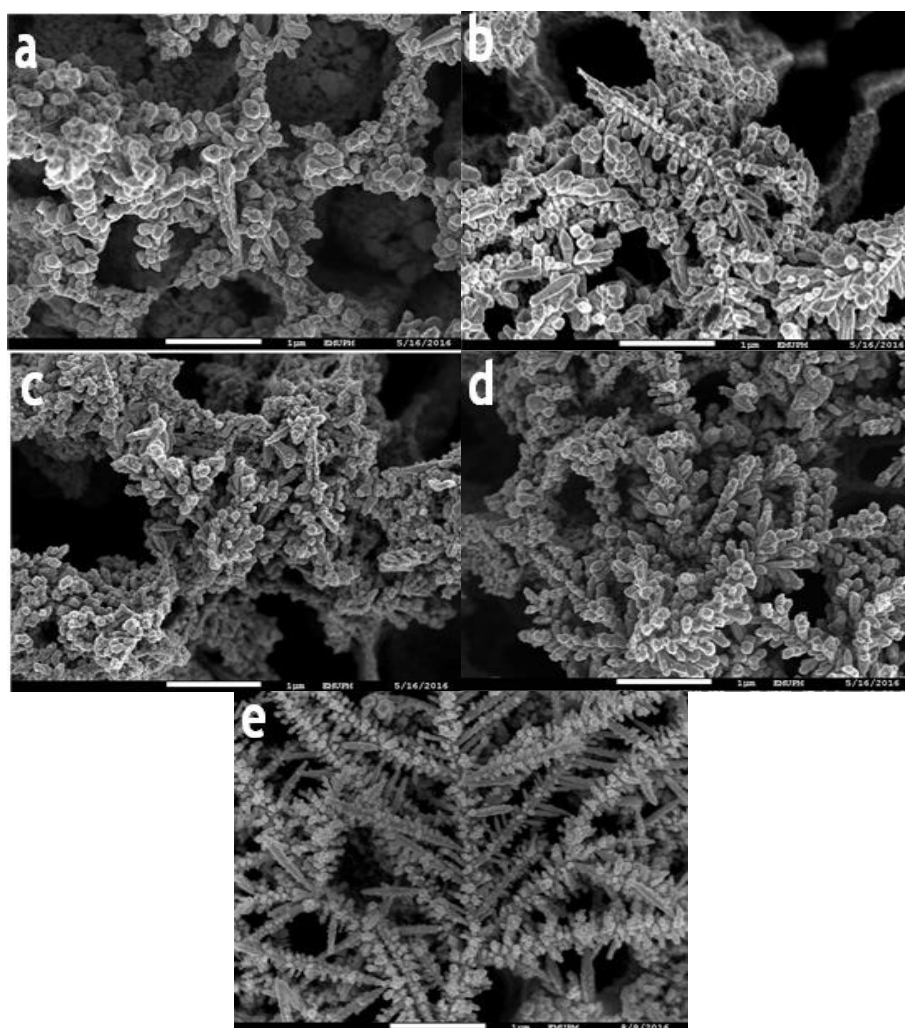


Fig. 3. FESEM of PS/Cu composite at different deposition current of (a) 1.42 mA cm<sup>-2</sup>, (b) 2.8 mA cm<sup>-2</sup>, (c) 5.6 mA cm<sup>-2</sup>, (d) 11.4 mA cm<sup>-2</sup> and (e) 14.2 mA cm<sup>-2</sup>.

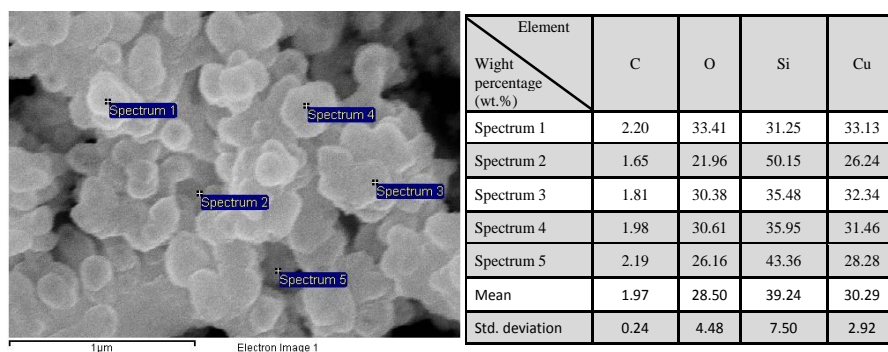


Fig. 4. EDX analysis of PS/Cu composite fabricated at  $DC = 1.4 \text{ mA/cm}^2$ .

#### 4. Photoluminescence Spectroscopy

Fig. 5 shows the PL curves obtained at excitation wavelength of 400 nm for pure PS and Cu deposited on PS at different DCs ( $1.4 - 14.2 \text{ mA cm}^{-2}$ ). To elucidate the role of Cu deposition, and accurately determined the peaks locations, all PL curves were fitted using Gauss function. The PS shows broad and intense PL emission peak centered at 604 nm. This large broadening peak indicated wide range distribution of Si crystal size. According to quantum confinement effect, the emission from Si grain at particular wavelength is dependence on its size [39]. By incorporate Cu in PS matrix, the PL peaks position, width and intensity were clearly changed [40]. Besides, two emission peaks were observed at around 570 and 530 nm. These peaks are related to Cu and  $\text{Cu}_2\text{O}$  nanoparticles that observed in XRD result[25]. These peaks were clearly enhanced by increasing DC. The emission related to PS crystals were strongly quenched at  $DC = 1.4 \text{ mA/cm}^2$ . This is probably due to formations of thick layer Cu crystals as indicated from XRD, (Table 1) that screen the emission from Si crystals (Cu crystallites size increased from 25.5 nm at  $DC 1.4 \text{ mA/cm}^2$  to 75.5 nm at  $DC = 5.6 \text{ mA/cm}^2$ ). The PL emission of PS has a slight blue shift to  $\sim 600 \text{ nm}$  for PS/Cu samples while its FWHM reduced with increasing DC. The average grains size of PS defines the position of the maximum of emission (center of the peak), while the width of the emission peak will be related to distribution of crystallite sizes [39]. Thus, it is believed that the reduction in the FWHM of the PL peak in PS/Cu composites could be due to the microstructure change of the nano-crystallites silicon (nc-Si) in PS layer modified by the deposited copper and copper oxide layer at varied DC. This mean that the size of nc-Si getting more uniform at high DC 11.4 and 14.2  $\text{mA/cm}^2$ . Again, the PL peak get enhanced with increasing DC which could be due to the decrease of crystallite size of Cu (crystallite size of Cu decreased from 75.5 nm at 5.6  $\text{mA/cm}^2$  to 21 for 14.2  $\text{mA/cm}^2$ ) that allow more emission from Si crystals.

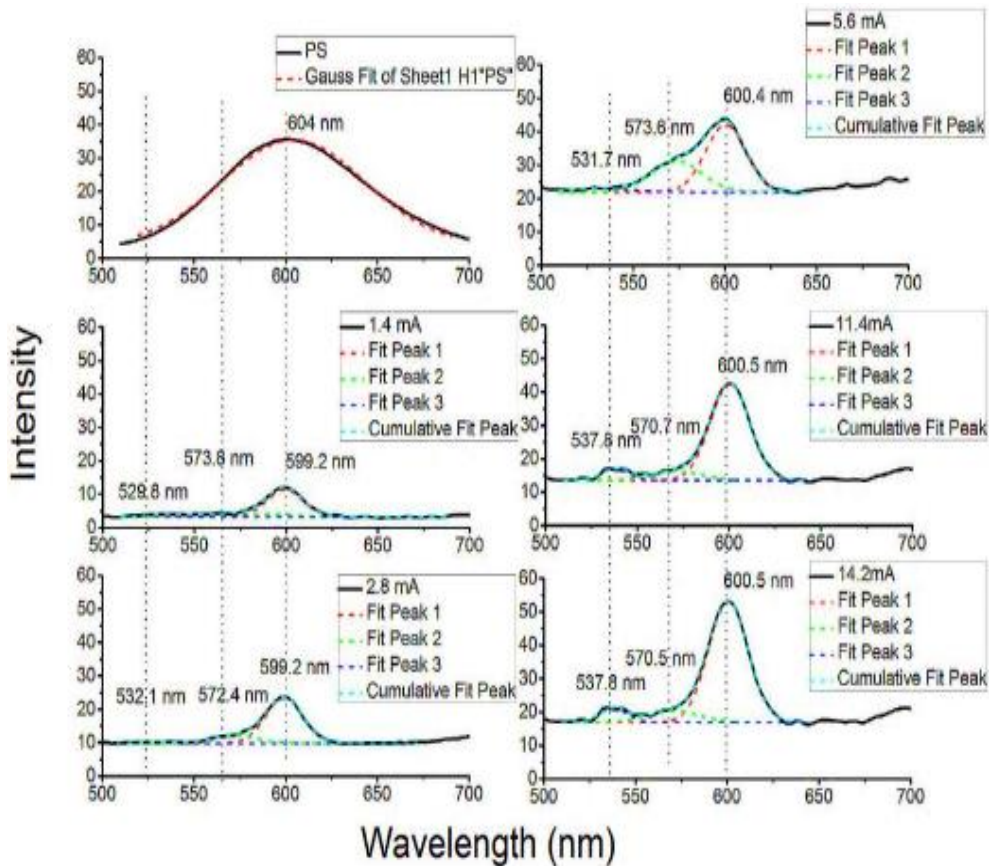


Fig. 5. PL of PS/Cu composites samples under different current densities  $DC = 1.4, 2.8, 5.6, 11.4$  and  $14.2 \text{ mA/cm}^2$ . Gaussian fitting of PS/Cu composites deposited are represented by dash coloured lines.

## 5. Device fabrication and testing

Fig. 6 demonstrates the I-V characteristic of CuO /PS device measured under illumination and dark at room temperature. For the purpose of comparison, the MSM device based on the bare PS has also been fabricated (named reference) Fig.6 a. All the I-V curves show typical Schottky diode-like behaviors due to the formation of hetero-junctions structures between the CuO and PS, also between PS and Si substrate. The MSMs response increases with increase the bias voltage, and is gradually saturated at high voltage value. At low voltage, the starting current is typically from thermionic emission current. The thermionic emission in the linear region and the velocity of carriers increases with the increase in biasing voltage. The saturation of dark current and the photocurrent are caused by sweeping out of all carriers toward the contact. Under forward bias, the potential barrier at the CuO /PS interface is lowered, resulting in a large flow of majority carries, thereby enhancing the dark current ( $I_d$ ). The reverse current density of the device increases under illumination due to the generation and collection of photo excited minority carriers. CuO /PS MSM exhibited more significant changes to the dark current characteristics compared to reference sample PS/Si device. This finding was further confirmed by measuring the contrast ratio of photocurrent and dark current at 5 V. The contrast ratio for CuO /PS MSM and reference MSM were found to be 63 and 3 respectively. In addition, in the case of the CuO /PS MSM, the observed saturation current density ( $I_0$ ) is fairly small in comparison to reference device, also, the highest photo-current is produced by the CuO /PS PD( Table 2). This shows that the illumination can effectively create e-h pairs in CuO /PS junction and greatly increase the carrier density. Besides, the existent of PS arrays significantly increased the interface area [41] between CuO and PS, and the three dimensional nature of CuO arrays largely improved the light absorption. Simultaneously, the engineered CuO/PS electronic structure at interface and electron transport channels of the CuO

both contributed to the efficient separation of photo-induced charges, therefore resulting in the enhanced photocurrent ( $I_{ph}$ ). In respect to reference device, the resistance of PS layer controls the characteristics of the PD, which is responsible for the reduction of current flow. Using the standard diode equation given below, the diode properties of the fabricated devices were determined.

$$I = I_0 \text{Exp} \left[ \frac{qv}{nK_B T} \right] \quad (6)$$

where  $I_0$  is saturation current,  $n$  is the ideality of any fabricated device,  $T$  is absolute temperature,  $K$  is Boltzmann constant,  $q$  is the elementary electronic charge,  $V$  is the applied voltage. The ideality of fabricated devices is given by the slope of the liner region of the semilogarithmic forward bias  $I$ - $V$  curve and expressed by

$$n = \frac{q}{KT} \left( \frac{dV}{d(\ln I)} \right) \quad (7)$$

The  $n$  value signify the non-ideal behavior of the PS device, which is probably due to the both strong parasitic generation and recombination at the interface states. The lattice mismatch between layers and/or the tunneling processes caused by interface states can greatly enhance the recombination and the parasitic generation rates[42]. The diode ideality factor of the present CuO /PS heterojunction is too far from that reported for the ZnS/Si nanowire radial heterojunction ( $n=11.3$ )[43], the CuS/Si cone-like radial heterojunction ( $n=8.2$ )[44], the ZnS/PS heterojunction ( $n=83$ ) and the ZnO/PS heterojunction ( $n=95$ ) [45]. The  $n$  value of CuO /PS device under high annealing condition  $350^\circ\text{C}$  are the nearest to unity, due to increases the crystallinity along with annealing, flexible three-dimensional structure and large surface area of the CuO/PS can reduce the structural disorders formed in the CuO films and hence, the formation of extended defects/dislocations resulting from the lattice mismatch may disappear.

Table 2. Summarizes the electrical measurements at 5 V, saturation current, and ideality factor for PS/Si and CuO /PS junctions.

Sample	Environmental conditions	Ideality factor $n$	Current at 5 V	Contrast ratio	Saturation current $I_0$ (A) under light
Reference devices PS/Si	Dark	4.1	$1.3 \times 10^{-4}$	3	$2.55 \times 10^{-7} \pm 0.02$
	Illumination	4.0	$3.6 \times 10^{-4}$		
CuO/PS( $350^\circ\text{C}$ )	Dark	1.7	$2.1 \times 10^{-5}$	63	$1.66 \times 10^{-8} \pm 0.05$
	Illumination	1.6	0.0013		

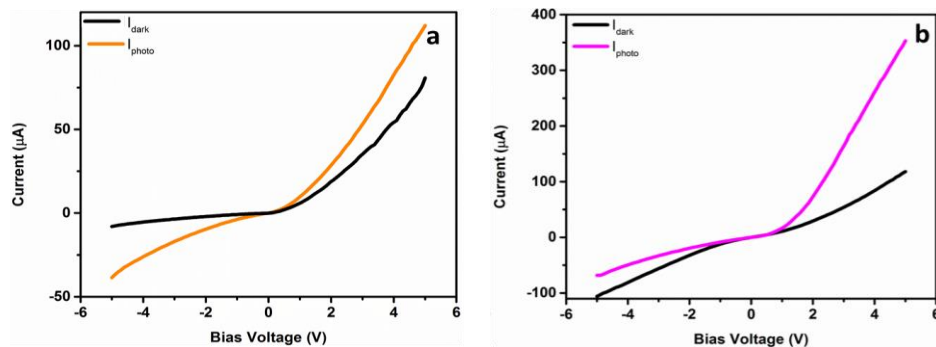


Fig. 6.  $I$ - $V$  characteristics of MSM PDs under dark and illumination conditions of (a) PS/Si device, and (b) CuO /PS device.

### 5.1. Photoresponse (ON-OFF) Measurements

The dynamic photo response of the CuO /PS and PS devices has been tested by turning ON and OFF the blue light under 0.5 V, 1V and 3 V bias voltage at regular intervals. The corresponding increase in photocurrent as a function of time at different bias voltages for devices is shown in Fig. 7. The photocurrent decay under illumination conditions without showing a pronouncing photocurrent tail suggests that the devices have good carrier transport properties.

The photoresponse spectra of the PDs can be related to the crystallinity, defect ratio and barrier height of devices [46]. Therefore, the photoresponse results is in agreement with XRD result indicating the good crystallinity of the sample prepared under annealing temperatures of 350°C. It is interesting to note that the transient response characteristics of the CuO /PS PD is step-like, showing distinct saturating behavior with significant increase in the saturated photocurrents even at low bias voltage compared to reference device PS. This finding was further confirmed by measuring the photosensitivity  $(S) = ((I_{ph} - I_d)/I_d) \times 100$  of photocurrent and dark current at 3V for devices, see Table 3. The photosensitivity value for CuO /PS PD and reference PS PD were found to be 660 and 180, respectively. The observed enhancement in the photocurrent of the CuO /PS diodes under the blue light illumination was much more than that obtained for the reference diode PS, is attributed to the modulation of the depletion region to a large extent at the interface of the CuO nanodendrites and PS arrays under illumination in the case of the composite device CuO /PS. The photoconduction in CuO /PS is due to the photo-induced chemidesorption of oxygen (trap centers for conduction electrons) primary embedded at the grain boundaries. In the beginning, an observation was made of lower base line dark current, which may be attributed to the trapping of free electrons at the surface of nano-dendrite by the absorption of atmospheric oxygen [47]. These negatively charged surface states introduced a depletion region near the surface, which result to a lower current before illumination. Under blue light irradiation, there is the creation of a large number of electron-hole pairs at the surface. The photo generated holes recombine with the chemisorbed oxygen ions (trapped charge carriers) on the surface and eliminate the depletion region. Thereby, increasing the concentration of electrons in the conduction band of the CuO nanodendrites, giving an enhanced value of the photocurrent [48].



The saturating nature of the photocurrent manifests that the equilibrium of the transition of charge carriers between the conduction band and defect levels has occurred very swiftly. Under blocking the irradiation of blue light, the photocurrent decays rapidly to the initial dark current level due to the recombination photo-generated charge carriers (free electrons) captured at the trap centers [49]. For the CuO /PS, the decay of current is also faster due to the high rate of photogenerated electron-hole pairs (solid-state process) and gas reabsorption (surface effects) recombination at the surface [50];[51][52].



The rise time (i.e., the time in which current increased from 10% to 90% of its saturation value) and decay time (i.e., the time in which current decreased from 90% and back to 10% of its saturation value) for all devices were measured at 3 V and summarized in Table 3. The response time and recovery time in the present work of the CuO nanodendrites /PS device revealed the shortest value as compared to those achieved by others researchers, where Kar et al. successfully fabricated ZnO nanowires/PS heterostructure detector, but with a very slow decay time (100 s)

[50]. Recently, Akgul et al. fabricated CuO/PS nanowire heterojunction photodiode, but with poor response and recovery time ( $\sim 1$  s) [53].

The fast response time that is obtained of CuO /PS detectors is attributed to the good quality and big photo-active surface areas of the samples. The fast response is associated with the short transit time of photo-generated carriers with long lifetime [54];[55]. Moreover, the photoresponse time is a factor of the traps centers present in the sensing material. The lower time constant can be achieved by increasing the surface to volume ratio [56]. Furthermore, the time constant also depends on both energy and intensity of the illuminated lamp [57].

Table 3. The rise time, fall time and photosensitivity of PS/Si device, and of CuO /PS devices.

Sample	Rise Time (ms)	Fall Time (ms)	Photosensitivity (S)
Reference devices PS	87	73	180
CuO/PS(350 °C)	80	80	660

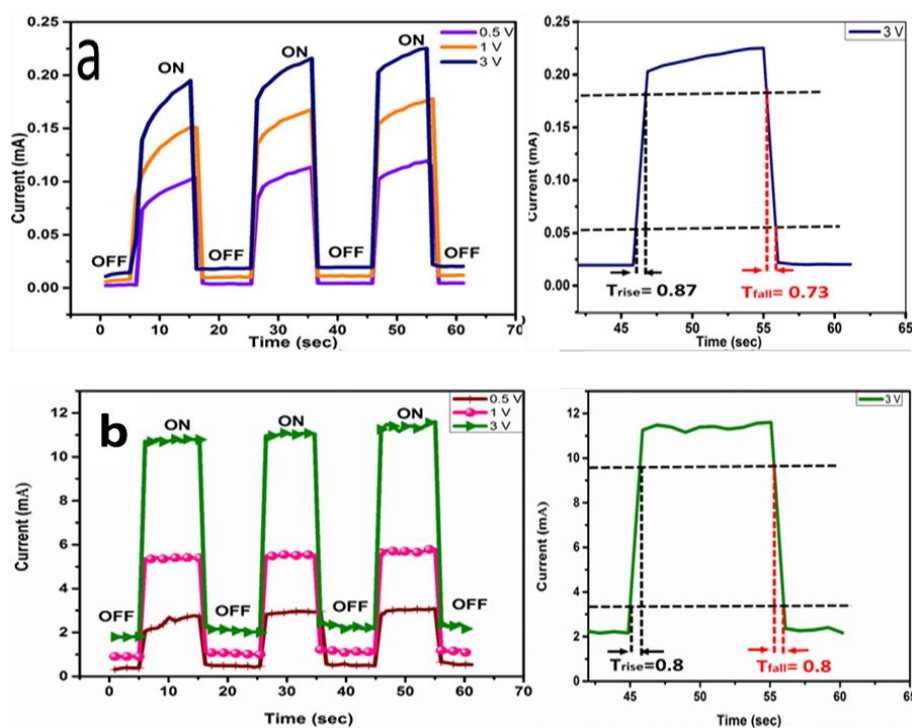


Fig. 7. Repetitive switching under blue light at different bias voltages of (a) PS/Si device, and (b) CuO /PS device.

## 6. Conclusions

Nano-dendrites PS/Cu composites were successfully fabricated using an electrochemical deposition. The size and shape of Cu formed on PS was strongly affected by the DC of the electrochemical deposition. XRD spectra confirmed the formation of the PS/Cu where the peak of Cu (111) arisen as the most prominent peak. The samples contain cubic Cu phase with crystallite size in the range of 22 to 97 nm. At lower Dc the growth rate was either too low and no dendrite shape formation took place.

The dendrite shape was found to grow well at cathodic current of 11.4 and 14.2 mA/cm<sup>2</sup>. Most of Cu ions accumulate on top of the Si silkstone and decrease inside the pore. The PL peak spectra was enhanced and getting narrower at high DC 14.2 mA/cm<sup>2</sup> which is promised property

for photodetector devices application. Under optimum conditions, the MSM photodetectors with high work function Pt metal of PS/Si and CuO-NDs/PS samples have been fabricated and characterized. The obtained measurement and calculated results have supported the optimum sample for fabricating the best photodetector devices.

### Acknowledgements

This work was supported by the Ministry of Higher Education Malaysia under Research University Grant Scheme Grant No. (GP-IPB/2014/9449900).

### References

- [1] L. T. Canham, "Silicon quantum wire array fabrication by electrochemical and chemical dissolution of wafers," *Appl. Phys. Lett.*, vol. 57, no. 10, pp. 1046–1048, 1990.
- [2] M. V. Wolkin, J. Jorne, P. M. Fauchet, G. Allan, and C. Delerue, "Electronic States and Luminescence in Porous Silicon Quantum Dots: The Role of Oxygen," *Phys. Rev. Lett.*, vol. 82, no. 1, pp. 197–200, 1999.
- [3] V. Lehmann, B. Jobst, T. Muschik, A. Kux, and V. Petrova-Koch, "Correlation between Optical Properties and Crystallite Size in Porous Silicon," *Jpn. J. Appl. Phys.*, vol. 32, no. 5R, p. 2095, 1993.
- [4] P. Kumar, "Effect of Silicon Crystal Size on Photoluminescence Appearance in Porous Silicon," *ISRN Nanotechnol.*, vol. 2011, pp. 1–6, 2011.
- [5] Y. Kumar *et al.*, "Cathodoluminescence and photoluminescence of swift ion irradiation modified zinc oxide-porous silicon nanocomposite," *Mater. Sci. Eng. B*, vol. 177, no. 16, pp. 1476–1481, 2012.
- [6] F. Priolo, T. Gregorkiewicz, M. Galli, and T. F. Krauss, "Silicon nanostructures for photonics and photovoltaics," *Nat. Nanotechnol.*, vol. 9, no. 1, pp. 19–32, 2014.
- [7] R. Mentek, D. Hippo, B. Gelloz, and N. Koshida, "Photovoltaic effect with high open circuit voltage observed in electrochemically prepared nanocrystalline silicon membranes," *Mater. Sci. Eng. B Solid-State Mater. Adv. Technol.*, vol. 190, pp. 33–40, 2014.
- [8] B. E. B. Al-Jumaili *et al.*, "Responsivity Dependent anodization current density of nanoporous silicon based MSM photodetector," *J. Nanomater.*, vol. 2016, 2016.
- [9] B. E. B. Al-Jumaili, Z. A. Talib, J. L. Y., S. B. Paiman, and N. M. Ahmed, "Photoelectric properties of metal-semiconductor-metal photodetector based on porous silicon," *J. solid state Sci. Technol. Lett.*, vol. 17, no. 1, pp. 79–82, 2016.
- [10] C. C. Chang and C. Chen, "A new process for the fabrication of silicon-on-insulator structures by using porous silicon," *Mater. Lett.*, vol. 32, no. September, pp. 287–290, 1997.
- [11] L. Luo *et al.*, "Er/Yb Doped Porous Silicon—A Novel White Light Source," *Adv. Mater.*, vol. 16, no. 18, pp. 1664–1667.
- [12] A. S. Lenshin *et al.*, "Composition of nanocomposites based on thin layers of tin on porous silicon formed by magnetron sputtering," *Phys. B Condens. Matter*, vol. 504, pp. 1–8, 2017.
- [13] T. S. T. Amran, M. R. Hashim, N. K. A. Al-Obaidi, H. Yazid, and R. Adnan, "Optical absorption and photoluminescence studies of gold nanoparticles deposited on porous silicon," *Nanoscale Res. Lett.*, vol. 8, no. 1, p. 35, Jan. 2013.
- [14] R. Jiang, X. Du, W. Sun, Z. Han, and Z. Wu, "Enhancement of the blue photoluminescence intensity for the porous silicon with HfO<sub>2</sub> filling into microcavities," *Sci. Rep.*, vol. 5, 2015.
- [15] H. A. R. A. Hassan, M. A. M. Hassan, and I. R. Agool, "Construction of semiconductor nanocomposite on porous silicon using chemical method," *Opt. - Int. J. Light Electron Opt.*, vol. 127, no. 23, pp. 11411–11417, 2016.
- [16] R. G. Singh, F. Singh, D. Kanjilal, V. Agarwal, and R. M. Mehra, "White light emission from chemically synthesized ZnO-porous silicon nanocomposite," *J. Phys. D: Appl. Phys.*, vol. 42, no. 6, p. 62002, 2009.
- [17] N. I. Rusli, M. Tanikawa, M. R. Mahmood, K. Yasui, and A. M. Hashim, "Growth of High-Density Zinc Oxide Nanorods on Porous Silicon by Thermal Evaporation," *Materials (Basel)*, vol. 5, no. 12, pp. 2817–2832, Dec. 2012.
- [18] P. Granitzer, K. Rumpf, P. Pöhl, S. Šimić, and H. Krenn, "Formation of self-assembled metal/silicon nanocomposites," *Phys. status solidi*, vol. 205, no. 6, pp. 1443–1446.
- [19] P. Granitzer and K. Rumpf, "Porous silicon—a versatile host material," *Materials*, vol. 3, no. 2, pp. 943–998, 2010.
- [20] I. Zhitomirsky, "Cathodic electrodeposition of ceramic and organoceramic materials. Fundamental aspects," *Adv. Colloid Interface Sci.*, vol. 97, no. 1–3, pp. 279–317, 2002.
- [21] D. Lincot, "Electrodeposition of semiconductors," *Thin Solid Films*, vol. 487, no. 1–2, pp. 40–48, 2005.
- [22] Y. H. Ogata, K. Kobayashi, and M. Motoyama, "Electrochemical metal deposition on silicon," *Curr. Opin. Solid State Mater. Sci.*, vol. 10, no. 2006, pp. 163–172, 2006.
- [23] D. Gallach, A. Muñoz-Noval, V. Torres-Costa, and M. Manso-Silván, "Luminescence and fine structure correlation in ZnO permeated porous silicon nanocomposites," *Phys. Chem. Chem. Phys.*, vol. 17, no. 32, pp.

- 20597–20604, 2015.
- [24] Y. M. Huang, “Photoluminescence of copper-doped porous silicon,” *Appl. Phys. Lett.*, vol. 69, no. 19, pp. 2855–2857, 1996.
- [25] X. Lu, Y. Ishida, and T. Yonezawa, “Synthesis and fluorescence properties of columnar porous silicon: the influence of Cu-coating on the photoluminescence behaviour of hydrofluoric-acid-treated aged columnar porous silicon,” *New J. Chem.*, vol. 39, no. 8, pp. 6267–6273, 2015.
- [26] A. A. Ensafi, M. M. Abarghoui, and B. Rezaei, “A new non-enzymatic glucose sensor based on copper/porous silicon nanocomposite,” *Electrochim. Acta*, vol. 123, pp. 219–226, 2014.
- [27] K. Fukami, Y. Tanaka, M. L. Chourou, T. Sakka, and Y. H. Ogata, “Filling of mesoporous silicon with copper by electrodeposition from an aqueous solution,” *Electrochim. Acta*, vol. 54, no. 8, pp. 2197–2202, 2009.
- [28] B. E. B. Al-Jumaili *et al.*, “Impact of ablation time on Cu oxide nanoparticle green synthesis via pulsed laser ablation in liquid media,” *Appl. Phys. A*, vol. 124, no. 9, p. 577, 2018.
- [29] G. Oskam, J. G. Long, A. Natarajan, and P. C. Searson, “Electrochemical deposition of metals onto silicon,” *J. Phys. D. Appl. Phys.*, vol. 31, no. 16, pp. 1927–1949, 1998.
- [30] G. Filipič and U. Cvelbar, “Copper oxide nanowires: a review of growth,” *Nanotechnology*, vol. 23, no. 19, p. 194001, 2012.
- [31] P. Poizot, C.-J. Hung, M. P. Nikiforov, E. W. Bohannon, and J. A. Switzer, “An Electrochemical Method for CuO Thin Film Deposition from Aqueous Solutions,” *Electrochem. Solid-State Lett.*, vol. 6, no. II, pp. C21–C25, 2003.
- [32] X. Song, D. Xu, H. Yang, Z. Yu, and G. Qiu, “Ag Deposition Forms and Uniformity on Porous Silicon by Electrochemical Method,” *Chinese J. Chem. Phys.*, vol. 23, no. 2, pp. 211–216, 2010.
- [33] N. G. Mistkawi, M. a. Hussein, M. Ziomek-Moroz, and S. B. Ranavavare, “Corrosion Behavior of Copper Thin Films in Organic HF-Containing Cleaning Solution for Semiconductor Applications,” *J. Electrochem. Soc.*, vol. 157, no. 1, p. C24, 2010.
- [34] L. C. Wang, N. R. de Tacconi, C. R. Chenthamarakshan, K. Rajeshwar, and M. Tao, “Electrodeposited copper oxide films: Effect of bath pH on grain orientation and orientation-dependent interfacial behavior,” *Thin Solid Films*, vol. 515, no. 5, pp. 3090–3095, 2007.
- [35] F. A. Harraz, T. Sakka, and Y. H. Ogata, “Immersion plating of copper using (CF<sub>3</sub>SO<sub>3</sub>)<sub>2</sub>Cu onto porous silicon from organic solutions,” *Electrochim. Acta*, vol. 46, pp. 2805–2810, 2001.
- [36] H. S. Shin, J. Y. Song, and J. Yu, “Template-assisted electrochemical synthesis of cuprous oxide nanowires,” *Mater. Lett.*, vol. 63, no. 3–4, pp. 397–399, 2009.
- [37] H. C. Shin, J. Dong, and M. Liu, “Nanoporous Structures Prepared by an Electrochemical Deposition Process,” *Adv. Mater.*, vol. 15, no. 19, pp. 1610–1614, 2003.
- [38] N. D. Nikolić, K. I. Popov, L. J. Pavlović, and M. G. Pavlović, “The effect of hydrogen codeposition on the morphology of copper electrodeposits. I. the concept of effective overpotential,” *J. Electroanal. Chem.*, vol. 588, no. 1, pp. 88–98, 2006.
- [39] R. J. Martin-Palma, L. Pascual, P. Herrero, and J. M. Martínez-Duart, “Monte Carlo determination of crystallite size of porous silicon from x-ray line broadening,” *Appl. Phys. Lett.*, vol. 87, no. 21, p. 211906, 2005.
- [40] A. Mabrouk, N. Lorrain, M. L. Haji, and M. Oueslati, “Correlation between optical properties surface morphology of porous silicon electrodeposited by Fe<sup>3+</sup> ion,” *Superlattices Microstruct.*, 2015.
- [41] Z. Kang *et al.*, “Electronic structure engineering of Cu<sub>2</sub>O film/ZnO nanorods array all-oxide p-n heterostructure for enhanced photoelectrochemical property and self-powered biosensing application,” *Sci. Rep.*, vol. 5, p. 7882, 2015.
- [42] L. Hao *et al.*, “Electrical and photovoltaic characteristics of MoS<sub>2</sub>/Si p-n junctions,” vol. 114502, 2015.
- [43] A. K. Katiyar, A. K. Sinha, S. Manna, and S. K. Ray, “Fabrication of Si/ZnS Radial Nanowire Heterojunction Arrays for White Light Emitting Devices on Si Substrates,” *Appl. Mater. Interfaces*, vol. 6, 2014.
- [44] A. K. Katiyar, A. K. Sinha, S. Manna, R. Aluguri, and S. K. Ray, “Optical photoresponse of CuS-n-Si radial heterojunction with Si nanocone arrays fabricated by chemical etching,” *Phys. Chem. Chem. Phys.*, vol. 15, no. 48, pp. 20887–20893, 2013.
- [45] C. Wang, B. Hu, and H. Yi, “The study of structure and optoelectronic properties of ZnS and ZnO films on porous silicon substrates,” *Optik (Stuttg.)*, vol. 123, pp. 1040–1043, 2012.
- [46] M. Z. Mohd Yusoff *et al.*, “AlN/GaN/AlN heterostructures grown on Si substrate by plasma-assisted MBE for MSM UV photodetector applications,” *Mater. Sci. Semicond. Process.*, vol. 29, pp. 231–237, 2015.
- [47] O. Lupan, L. Chow, G. Chai, L. Chernyak, O. Lopatiuk-Tirpak, and H. Heinrich, “Focused-ion-beam fabrication of ZnO nanorod-based UV photodetector using the in-situ lift-out technique,” *Phys. Status Solidi*, vol. 205, no. 11, pp. 2673–2678, 2008.
- [48] N. K. Hassan, M. R. Hashim, and N. K. Allam, “Low power UV photodetection characteristics of cross-linked ZnO nanorods/nanotetrapods grown on silicon chip,” *Sensors Actuators, A Phys.*, vol. 192, pp. 124–129, 2013.
- [49] S. M. Mohammad, Z. Hassan, N. M. Ahmed, N. H. Al-Hardan, and M. Bououdina, “Fabrication of low cost UV photo detector using ZnO nanorods grown onto nylon substrate,” *J. Mater. Sci. Mater. Electron.*, vol. 26, no. 3, pp. 1322–1331, 2015.
- [50] J. P. Kar, S. N. Das, J. H. Choi, Y. a. Lee, T. Y. Lee, and J. M. Myoung, “Fabrication of UV detectors based on ZnO nanowires using silicon microchannel,” *J. Cryst. Growth*, vol. 311, pp. 3305–3309, 2009.
- [51] X. Xie *et al.*, “Enhanced solar-blind responsivity of photodetectors based on cubic MgZnO films via gallium doping,” *Opt. Express*, vol. 22, no. 1, pp. 246–253, 2014.
- [52] Q. Zhang *et al.*, “CuO nanostructures: Synthesis, characterization, growth mechanisms, fundamental properties, and applications,” *Prog. Mater. Sci.*, vol. 60, pp. 208–237, 2014.

- [53] G. Akgul, F. A. Akgul, E. Mulazimoglu, H. E. Unalan, and R. Turan, "Fabrication and characterization of copper oxide-silicon nanowire heterojunction photodiodes," *J. Phys. D. Appl. Phys.*, vol. 47, no. February 2016, p. 065106, 2014.
- [54] H. I. Abdulgafour, Z. Hassan, F. K. Yam, K. Al-Heuseen, and Y. Yusof, "Enhancing photoresponse time of low cost Pd/ZnO nanorods prepared by thermal evaporation techniques for UV detection," *Appl. Surf. Sci.*, vol. 258, no. 1, pp. 461–465, 2011.
- [55] Y. Takahashi, M. Kanamori, A. Kondoh, H. Minoura, and Y. Ohya, "Photoconductivity of Ultrathin Zinc-Oxide Films," *Japanese J. Appl. Phys. Part 1-Regular Pap. Short Notes Rev. Pap.*, vol. 33, no. 12A, pp. 6611–6615, 1994.
- [56] Y. Feng, W. Hou, X. Zhang, P. Lv, Y. Li, and W. Feng, "Highly sensitive reversible light-driven switches using electrospun porous aluminum-doped zinc oxide nanofibers," *J. Phys. Chem. C*, vol. 115, pp. 3956–3961, 2011.
- [57] S. H. Abud, Z. Hassan, and F. K. Yam, "Fabrication and characterization of metal-semiconductor-metal photodetector based on porous InGaN," *Mater. Chem. Phys.*, vol. 144, pp. 86–91, Mar. 2014.